International Journal of Heat and Mass Transfer 149 (2020) 119120

Contents lists available at ScienceDirect

International Journal of Heat and Mass Transfer

journal homepage: www.elsevier.com/locate/hmt

An experimental investigation on the dynamic glaze ice accretion process over a wind turbine airfoil surface

Linyue Gao, Yang Liu, Hui Hu*

Department of Aerospace Engineering, Iowa State University, Ames, IA 50011-2271, United States

ARTICLE INFO

Article history:
Received 8 July 2019
Revised 8 November 2019
Accepted 25 November 2019

Keywords:
Ice accretion process
Water transport behavior
Wind turbine icing
Glaze ice
Digital Image Projection (DIP) technique

ABSTRACT

Icing events, particularly under precipitation-icing conditions in which high-liquidity glaze ice tends to form, could pose significant threats to the safe and effective operations of wind turbines in cold and wet environments. During the glaze ice accretion process, the wind-driven unfrozen water was coupled with the growth of ice structures and difficult to be quantified and characterized. In the present study, we introduced a Digital Image Projection (DIP) technique to quantitatively measure the unsteady water runback behaviors and dynamic ice accretion process under typical glaze icing conditions over a highly-cambered wind turbine airfoil surface, i.e., the pressure-side surface of DU91-W2-250 airfoil, in the Icing Research Tunnel at Iowa State University (ISU-IRT). DIP measurement results were found to be able to successfully capture the time-resolved three-dimensional information of the water transport behaviors over the ice accreting surface of the airfoil model during the glaze icing processes. The stumbling motions of the rivulet flows were observed during the icing processes, coupled with an increasing fluctuations induced by the underneath ice roughness. The forces acting on the rivulet flows were analyzed, and a theoretical model based on the force balance was built to predict the rivulet flows. The effects of the incoming airflow velocity on the glaze icing process over the airfoil surface were also studied, and it was found that, as the incoming flow velocity increased, the runback rivulet flows would move farther downstream and became thinner and narrower due to the increased aerodynamic stress acting on them. The rivulet bulged shape was found to have an inverse relationship with the inflow velocity squared. In addition, the ice accreted over the airfoil surface during an icing process was quantitatively decoupled from the unfrozen wind-driven water, and the quantitative results can be used to validate and optimize current ice accretion models.

1. Introduction

Wind energy has been globally regarded as the mainstream energy source for electricity production with competitive feed-in tariff with traditional fossil fuels since 2018. However, approximately 30% of wind turbines are threatened by various icing events in winter [1–4]. From the perspective of icing physics, there are two types of ice, i.e., rime ice and glaze ice [5]. Different from rime ice that forms immediately upon the impingement, only a portion of the impinged super-cooled water droplets would freeze upon impact during the glaze icing process, and the remaining droplets coalesce and run back driven by airflows [6,7], as shown in Fig. 1. Due to the high adhesion and complicated shapes caused by the wet nature, glaze ice is usually considered as the most dangerous type of ice [8–11]. Icing events can be generally categorized into two types, i.e., in-cloud icing and precipitation icing. In-cloud icing happens when the supercooled water droplets suspended in freezing fog impact the rotating wind turbine blades. The water droplets are usually small, and the median volumetric diameter (MVD) of water droplets is approximately 10–50 μm. Precipitation icing usually occurs accompanied by freezing drizzle (MVD = 50–500 μm), freezing rain (MVD = 500–4000 μm) or wet snow [12,13]. In comparison to in-cloud icing, precipitation icing with larger airborne water droplets is more prone to generate severe glaze ice over wind turbine blade surfaces, which may severely affect the safe and effective operations of wind turbines.

Most of the previous studies on wind turbine icing [6,8,14–17] are focused on in-cloud icing. The underlying icing physics of the high-liquidity precipitation icing (i.e., glaze icing process) is not clear. The high mobility of unfrozen water makes it very difficult to accurately predict the three-dimensional ice shapes and the dynamic motions of the film/rivulet flows during a glaze ice accretion process. Rothmayer et al. [18] developed a boundary layer theory to describe the water film runback on an airfoil surface based

* Corresponding author.
E-mail address: huhui@iastate.edu (H. Hu).

https://doi.org/10.1016/j.ijheatmasstransfer.2019.119120
0017-9310/

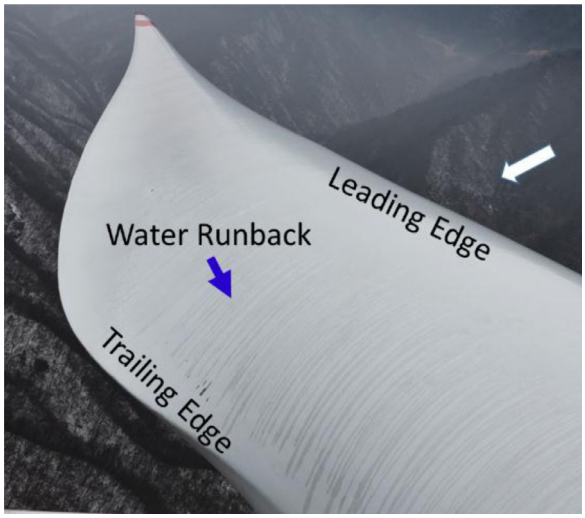

Fig. 1. A photo of the water runback behaviors taken at the beginning of a glaze icing process over the pressure-side blade surface of a 2 MW wind turbine.

on critical film thickness. Khalil et al. [19,20] proposed a runback model with the concept of the breakup of liquid film into individual rivulets. Following Khalil's work, Fortin et al. [21] used a mass balance model to determine the mass of ice and runback water with the known water state and maximum bead height. The aforementioned models play important roles in elucidating the underlying water runback physics and predicting the one/two-dimensional geometries of runback water flows during glaze ice formation and accretion process.

To further develop and validate the theoretical models, more comprehensive experimental data, particularly the time-resolved three-dimensional data, for the high-liquidity icing process are highly desirable. The dynamics, i.e., the stumbling runback motions, of a wind-driven droplet/rivulet flow over a flat plate surface was measured by using a digital fringe projection (DFP) technique by Hu et al. [22]. Soon after that, the DFP technique was further developed by Zhang and Hu [23] into a digital image projection (DIP) technique by replacing the white and black fringes with grid patterns. The DIP technique was then applied to investigate the unsteady film/rivulet flows over a NACA0012 airfoil under room temperature, and the leading-edge film thickness was found to follow the Nelson's scaling law very well [7,23,24]. The DIP technique was proved to be able to quantify the dynamics of film/rivulet flows, and here, it is suggested to be applied to high-liquidity icing-related studies for wind turbine icing applications.

In the present study, the DIP technique was applied to quantitatively measure the time-resolved three-dimensional shapes of the ice structures and film/rivulet flows accreted over a highly-cambered wind turbine airfoil surface under typical glaze icing conditions. Several freezing drizzle conditions were duplicated in the Icing Research Tunnel at Iowa State University (ISU-IRT) by manipulating the incoming flow velocity (V_∞), ambient air temperature (T_∞), liquid water content (LWC) level and MVD. Section 2 illustrates the detailed information of the principle of DIP technique and the experimental setup for the DIP measurements. Section 3 shows the instantaneous DIP measurement results and quantitatively analysis of the dynamic glace icing processes with various oncoming airflow velocities, followed by a simplified theoretical model based on force balance. Section 4 concludes the main findings derived from the present study that can be used to validate and optimize the existing ice accretion/water transport models and to provide a fundamental insight to develop effective and economic anti-/de-icing strategies for wind turbine mitigation in cold and wet environments.

2. Experiments

2.1. Principle of DIP technique

Digital Image Projection (DIP) technique is a non-intrusive structured light technique that can be used to reconstruct the three-dimensional (3D) features of an object. DIP technique was developed for the measurements of surface water transport over an airfoil surface by Zhang and Hu [23], and further optimized by Liu et al. [25] to measure the surface water/ice transport over an artificial-ice-roughened airfoil. Fig. 2 shows a schematic diagram of the principle of DIP technique. While a digital image projector is used to project grid patterns onto the reference plane, a high-speed camera is used to record the projected image patterns. When there is an object on the reference plane, the grid patterns will be deformed. The deformation has a linear relationship with the height/thickness of the object, as given in Eqs. (1) and (2). The camera and the projector are suggested to be installed at the same height. The ratio of the height of the object (H) to the vertical distance between the camera and the object (s-H) is proportional to the ratio of the displacement of the image pattern ($\overline{AB}$) to the distance between the camera and the projector ($\overline{MN}$, i.e., d) as given in Eq. (1). Since the height/thickness of the object is usually much smaller than the distance between the camera and the reference plane, the relationship of the height of the object and the displacement can be simplified from (s-H)/d to s/d, as given in Eq. (2).

$$\frac{d}{\overline{AB}} = \frac{s-H}{H} H = k\overline{AB},\ k \approx {}^{s}/_{d} \tag{2}$$

The displacement vectors are calculated based on the reference and deformed images by using a spatial cross-correlation image processing algorithm [23]. The displacement-to-height/thickness relationship (k) is a constant since the values of the vertical distance between the camera (s) and reference plane and the distance between the camera and the digital image project (d) are fixed for a DIP system. The displacement-to-thickness factor (i.e., k-map) can be determined through a calibration procedure similar to that

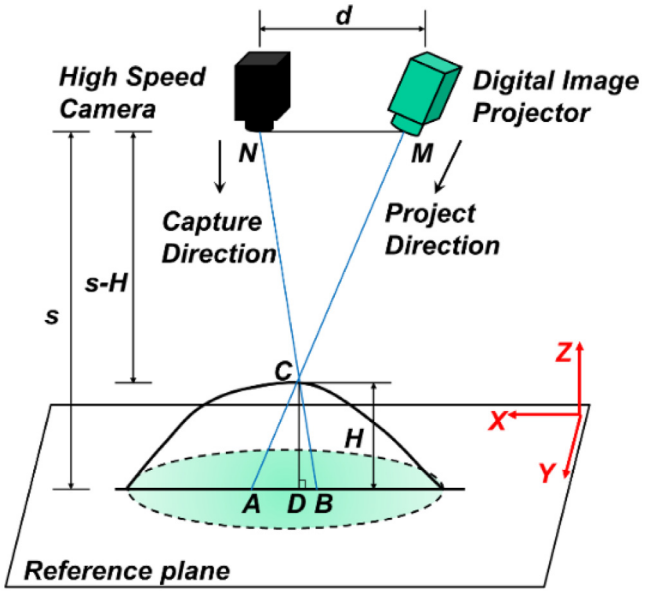

Fig. 2. A schematic diagram of the principle of the DIP technique.

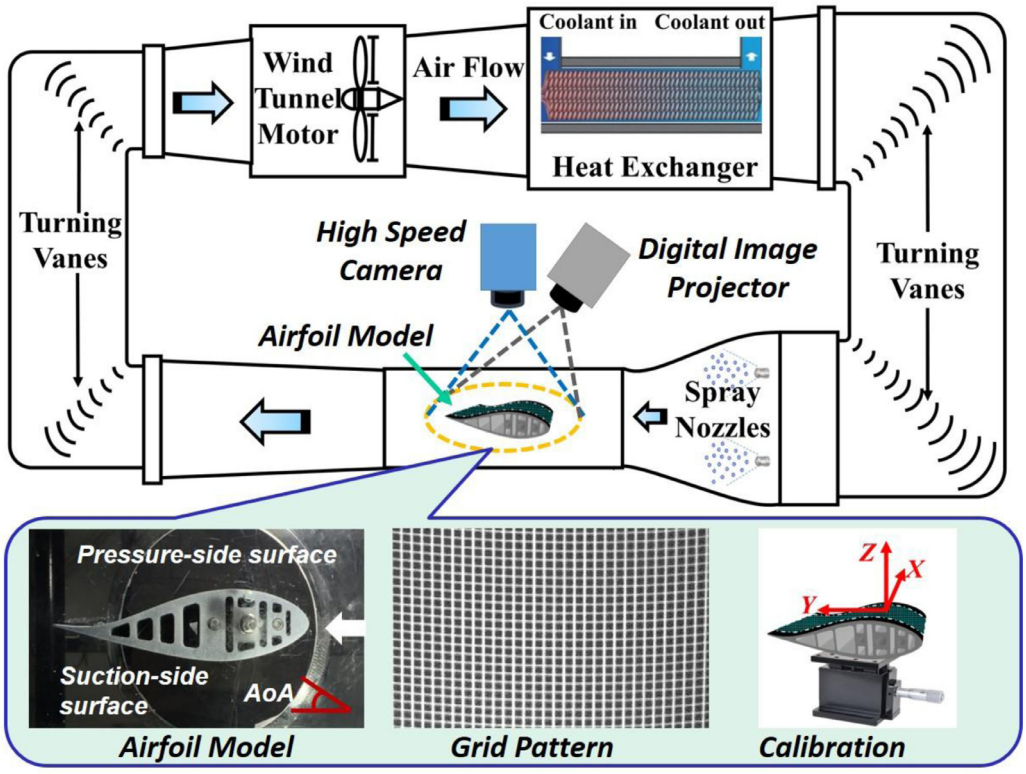

Fig. 3. A sketch of the experimental setup for quantifying the dynamic glaze icing processes over the pressure-side surface of a DU91-W2-250 airfoil model at ISU-IRT by using the DIP technique.

given in Zhang & Hu et al. [23]. As schematically shown in Fig. 3, a clean test model is mounted on top of a vertical translation stage (i.e., along z-direction) to adjust the height. The recorded images of the grid patterns on the test model at several pre-determined heights by the digital camera are processed by using the aforementioned spatial cross-correlation algorithm to acquire the displacement vectors of the grid patterns in reference to the image recorded with the test model placed at a pre-determined origin location of $z = 0$. At each point of interest, the slope of the linear relationship of the height and the image pattern displacement (i.e., k) is derived and used for the displacement to height/thickness conversion for DIP measurements. More detailed calibration procedure in the experiments are described in the following section. Based on the displacement information of the deformed image patterns and the displacement-to-height/thickness relationship (k), the height/thickness information of the object can be derived. With all the dimension information in x, y and z directions, the three-dimensional shape of the object can be reconstructed.

The DIP technique is an image correlation based technique and thus provides the spatially averaged measurement of a region. The spatial resolution of the DIP measurement is dominated by the interrogation window size for the cross correlation with the consideration of the measured displacement vector between the deformed and reference images [23]. Although we could use the width of the projected image lines for the grid patterns and the resolution of the image detection as the interrogation window size for the best spatial resolution, a larger size is suggested for a good accuracy level of the DIP measurements. In addition, the temporal resolution of the DIP measurement is determined by the exposure time for image acquisition. The uncertainty of the DIP measurements can be caused by various factors, including the important parameters of the DIP system such as the relative positions of the camera, the projector and the reference plane (i.e., the test model in the experiments), the resolutions of the digital camera and projector, the width of the projects grid lines, and the signal-to-noise ratio (SNR) of the acquired DIP images. The resolution of the translation stage used for DIP calibration procedure as well as the vibrations of the wind-loaded test model in the test section of the wind tunnel during the DIP measurements may also affect the uncertainty of the DIP measurements.

2.2. Experimental setup

In the present study, the representative icing events were simulated/duplicated in the Icing Research Tunnel at Iowa State University (ISU-IRT). ISU-IRT is a multifunctional research-grade icing tunnel that can duplicate a wide range of icing conditions that may take place on wind turbines in wet and cold environments [5,26,27]. The test section is 0.4 m × 0.4 m × 2.0 m with transparent side panels. As shown in Fig. 3, there are an array of pneumatic atomizing spray nozzles (Spraying Systems Co., 1/8NPT-SU11) installed at the entrance of the contraction section of the wind tunnel to produce water droplets impinging onto the test airfoil model installed in the middle of the test section. The liquid water content (LWC) level can be adjusted by regulating the flow rate through the nozzles. The median volumetric diameter (MVD) of the water droplets ranges from 10 μm to 100 μm depending on the combination of air pressure and water pressure through the spray nozzles. The small airborne water droplets can be quickly cooled down to the same temperature as the ambient airflow before they travel to the test section. The air temperature of the wind tunnel can be adjusted from −25 °C to the room temperature (~20 °C).

In the present study, a widely used wind turbine airfoil profile, i.e., DU91-W2-250, was selected to build the test airfoil model. DU91-W2-250 airfoil is an asymmetric, cambered, thick airfoil. The maximum thickness of this airfoil is 25% of its chord length (C).

To limit the thickness of the suction-side surface (i.e., the well-known upper surface) to control the upper surface velocities, the pressure-side surface (i.e., the well-known lower surface) was designed with an "S-shape" to simultaneously obtain the required thickness and sufficient lift [28]. The chord length and the span length of the airfoil model are 0.15 m and 0.40 m, respectively. The test airfoil model was 3D-printed by using a rapid prototyping machine with a hard-plastic material (i.e., VeroWhitePlus) that has similar thermal and structural properties to the materials used for wind turbine blades. The surface of the test airfoil model was coated with one layer of the finish paint (i.e., Rustoleum™, Flat Protective Enamel, white in color) and one layer of Primer underneath the finish paint. The surfaces of the test airfoil model were carefully polished with fine sandpapers up to 2000 grit to achieve a very smooth finish with about 25 μm in the characteristic roughness over the surface, and thus effects of the discretization of the airfoil surface was found to be trivial on the uncertainty budget of the DIP measurements. The airfoil model was supported with three stainless rods and could pivot around the ¼ of the chord length position (i.e., the aerodynamic center of the airfoil model).

Fig. 3 shows the experimental setup for the quantification of the dynamic glaze icing process over the DU91-W2-250 airfoil surface by using the DIP technique. The airfoil model was installed in the middle of the test section in the ISU-IRT with a angle of attack (AoA) of 5°, at which the airfoil model possesses the maximum lift-to-drag ratio as suggested by Timmer and van Rooij [29], which could be representative of wind turbine blade operating under the most efficient operation conditions. The pressure-side surface of the airfoil model with an AoA = 5°, in comparison to the suction-side surface, possesses the most prominent water film runback and rivulet formation information, and thus was selected in the present study to characterize the water transport behaviors over ice accreting airfoil model surface. The 360-degree information of ice structures accreted on the airfoil model (i.e., over both suction-side and pressure-side surfaces) at several instants were measured in our another study using a DIP-based 3D scanning system [30], which was not within the scope of the time-resolved water transport behaviors over the ice accreting airfoil surface given in the present study. It should be noted that the DU91-W2-250 airfoil model was mounted upside down with an AoA = 5° (i.e., pressure-side surface up, leading edge pivoting down) in the test section of ISU-IRT for an easy experimental setup, as shown in Fig. 3.

During the DIP measurement, while a digital image projector (DLP® LightCrafter™) was used to project grid patterns onto the airfoil model, a high-resolution camera (PCO Tech, Dimax Camera, 2K pixels × 2K pixels in resolution) with a 60 mm Macro-lens (Nikon, 60 mm Nikkor 2.8D), installed at the same height as the projector was used to acquire the snapshots of the deformed grid patterns caused by the water/ice structures accreted over the airfoil model surface during the dynamic glaze icing process. The framerate of the high-resolution camera for DIP image acquisition was set as 30 Hz with 2.0-ms exposure time that was proved to be adequate for characterizing the ice accretion process and water runback over an airfoil surface with freestream wind speeds lower than 40 m/s [23,31]. The width of the projected image lines used to generate the grid patterns was ~4 pixels (95% confidence interval in Gaussian distribution). The size of the grid pattern was set as 21 pixels × 21 pixels (i.e., 1.9 mm × 1.9 mm in physical space) for a good accuracy level. The size of the interrogation window for the spatial cross-correlation to determine the displacement vectors of the deformed images in reference to the reference image was 21 pixels × 21 pixels (the same as the grid pattern size) at the first stage and then refined to 7 pixels × 7 pixels for a better spatial resolution of ~ 0.6 mm to resolve the small-scale structures. In addition, a small amount of white latex paint (~ 1.0%) was added into the water sprays for the icing processes to increase the reflectance of the ice/water structures accreted over the airfoil surface.

Table 1
Test cases for characterization water transport behaviors over the ice accreting pressure-side surface of DU91-W2-250 airfoil model at AoA = 5°.

Case No.	Wind Velocity, V_∞	Air Temperature, T_∞	LWC
	[m/s]	[°C]	[g/m^3]
1	15	−5	6.7
2	20	−5	5.0
3	25	−5	4.0
4	30	−5	3.3

The calibration in z-direction was conducted following the aforementioned calibration procedures for the displacement-to-height/thickness conversion factors, i.e., k-map. The DU91-W2-250 airfoil model was fixed onto a vertical translation stage with pressure-side surface up at AoA = 5°, as shown in Fig. 3. The height of the airfoil model was adjusted by using the micrometer driver of the translation stage with a resolution of 10 μm. A series of snapshots with grid patterns at twenty uniformly spaced heights by 0.20 mm were acquired and used to calculate the displacement vectors based on the deformed information in reference to the reference image measured at the origin position of $z = 0$ (i.e., middle of the test section of ISU-IRT) with the aforementioned spatial cross-correlation algorithm. Fig. 4 shows the calibration results (i.e., the displacement-to-height/thickness conversion factors) in the projected area (around 150 mm × 100 mm in streamwise (y) and spanwise (x) directions). The average value of k was found to be approximately 0.22. The value of k was found to slightly vary in spatial of the projected area mainly due to the variations in the distance between the camera and the cambered airfoil surface.

Based on the displacement vectors calculated by the deformed image patterns in reference to the reference image and the displacement-to-height/thickness conversion factor (calibration k-map), the time-resolved the 3D water/ice structures were reconstructed. The uncertainty in the measured ice/water thickness of DIP measurement results was estimated to be ~ 150 μm.

2.3. Case design

Table 1 lists the test cases for the DIP measurements of the water transport behaviors over the ice accreting pressure-side surface of DU91-W2-250 airfoil model under typical glaze ice accretion conditions. Glaze ice was found to usually occur at relatively higher air temperatures, higher LWC and larger MVD, especially under the freezing drizzle condition, in comparison to the rime ice formation [32]. The air temperature was set as -5°C, a typical temperature for glaze ice formation, which could represent ~55% of icing events in winter as suggested by Hudecz [32]. The flow rate through the array of nozzles was set as 1000 mL/min to keep the same amount of impinging water in all the cases. The corresponding LWC levels ranged from 6.7 g/m^3 to 3.3 g/m^3, close to the actual operating conditions of wind turbines encountering with freezing drizzle/rain or other low-altitude high-water-content environments (such as ocean/sea spray) [33]. In the present study, by modulating the air pressure and water pressure supplied to the spray nozzles, the MVD of the airborne water droplets was set to be ~80 μm in order to simulate the atmospheric icing scenario with freezing drizzles. The velocity of the incoming airflow was varied from 15 m/s to 30 m/s with a step of 5 m/s in order to characterize the effects of wind speed on the water transport behaviors over ice accreting airfoil surface.

For each tested case, DIP measurements with 60 s in duration (i.e., 1800 images recorded with a framerate of 30 Hz) of the water

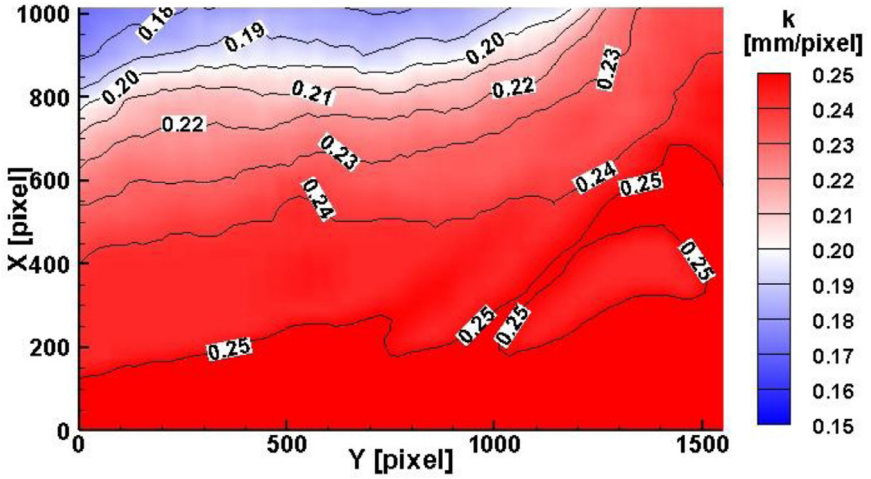

Fig. 4. Calibration map (i.e., displacement-to-thickness factor, k) for the DIP measurements of ice/water structures accreted over pressure-side surface of DU91-W2-250 airfoil model.

transport behaviors over the ice accreting airfoil surface under the aforementioned glaze icing conditions were conducted after the spray nozzles were turned on to inject water droplets into the airflow. The wind-driven water transport behavior over an airfoil and the involved heat transfer in course of the water solidification process were found to be stable within a quite short period of time of 15 s [23,34], and thus the selected 60-s measurement duration was believe to capable of capturing the most important phenomena of the water transport behaviors and ice accretion process over the airfoil surface.

3. Experimental results and discussion

3.1. Instantaneous icing process over an airfoil surface

Fig. 5 shows the acquired DIP images and the corresponding measurement result, including a reference image, a deformed image modulated by the accreted water/ice structures, and processed DIP measurement result of the water/ice structures over pressure-side surface of the airfoil model. Fig. 5(a) shows the reference image of the pressure-side surface of the clean DU91-W2-250 airfoil model with projected grid patterns. The grid patterns were uniform and regular-shaped, fitting the S-shape surface of the airfoil model very well. Fig. 5(b) shows one of the deformed images modulated by the ice structures and unfrozen water accreted over the surface. Fig. 5(c) shows the corresponding DIP measurement result of the three-dimensional shapes of the ice/water structures over the airfoil model surface. The contour shows the height/thickness (H) of the ice/water accreted over the airfoil surface. The DIP measurement result was found to be able to capture the water transport behaviors over the ice accreting airfoil surface very well. The signal-to-noise ratio (SNR, SNR = $20\log_{10}$ (signal/RMSnoise), where RMSnoise is defined as the square root of mean of variance from the background regions) in the DIP measurement results was found be ~ 48 dB for 150 μm ice/water structures, much higher than the suggested 20 dB for good SNR.

Fig. 6 shows the DIP measurement results of the time evolutions of the dynamic glaze icing processes over the pressure-side surface of DU91-W2-250 airfoil model with AoA = 5° at two typical incoming airflow velocities (i.e., 15 m/s and 30 m/s). Fig. 6(a) shows the instantaneous DIP measurement results of the dynamic icing process over the airfoil surface at V_∞ = 15 m/s. Six representative instants of the icing process were selected. At $t = t_0$, there were no water droplets impinging onto the surface, and the airfoil model was clean without any ice/water accretion. The height/thickness of the ice/water was all zero in the projected area. As time went on to $t = t_0 + 10$ s, the impinged water droplets onto the airfoil surface continued solidifying with tremendous latent heat of fusion releasing during the icing process. Since the heat transfer process over the airfoil surface under such a wet icing condition would not be able to remove/dissipate all the released latent heat of fusion immediately, only a portion of the impinged water droplets would be solidified and frozen into ice upon impact region near the airfoil leading-edge region. The remaining water driven by the airflow ran back to the farther downstream region, forming a thin film with the bulged front. The thickness of the film decreased as it advanced downstream. When the thickness of the film reached the minimum limitation defined in terms of

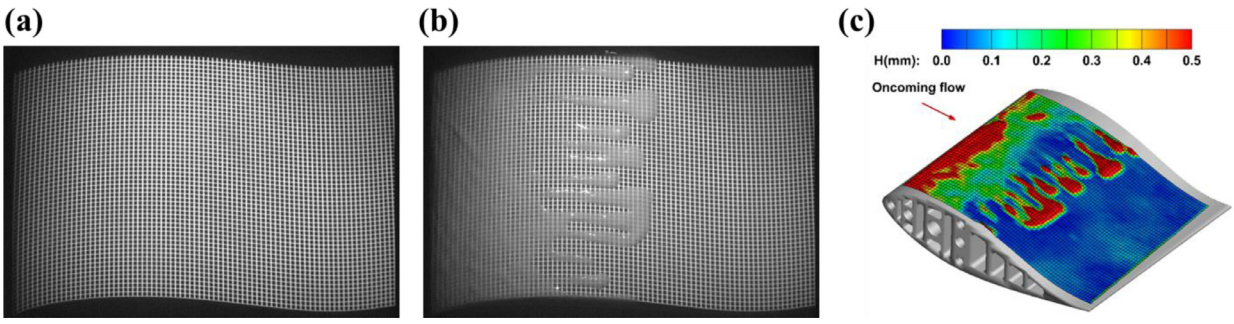

Fig. 5. Acquired DIP images and processed DIP measurement result for the study of water transport behaviors over the ice accreting airfoil surface. (a) Reference image; (b) Deformed image modulated by water/ice structures; (c) DIP measurement result of the water/ice structures over pressure-side surface of the airfoil model.

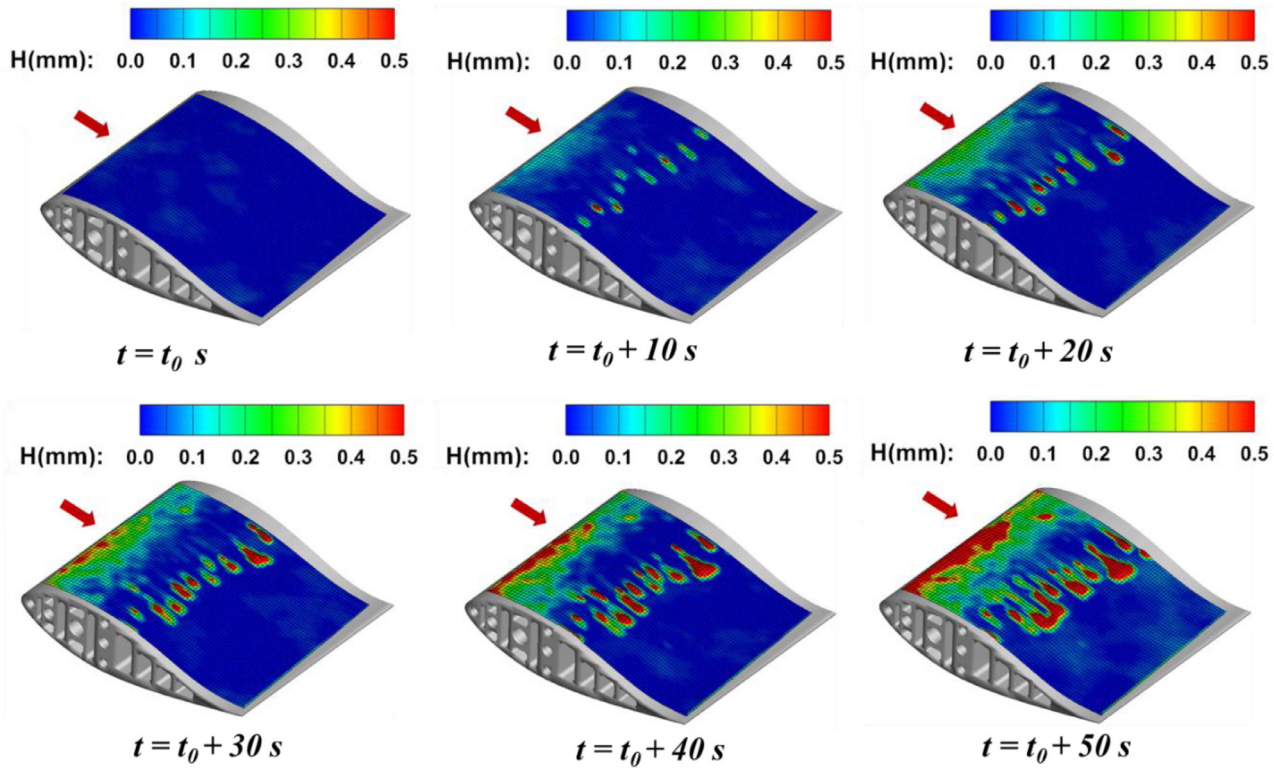

(a) DIP measurement results with V_∞ = 15 m/s.

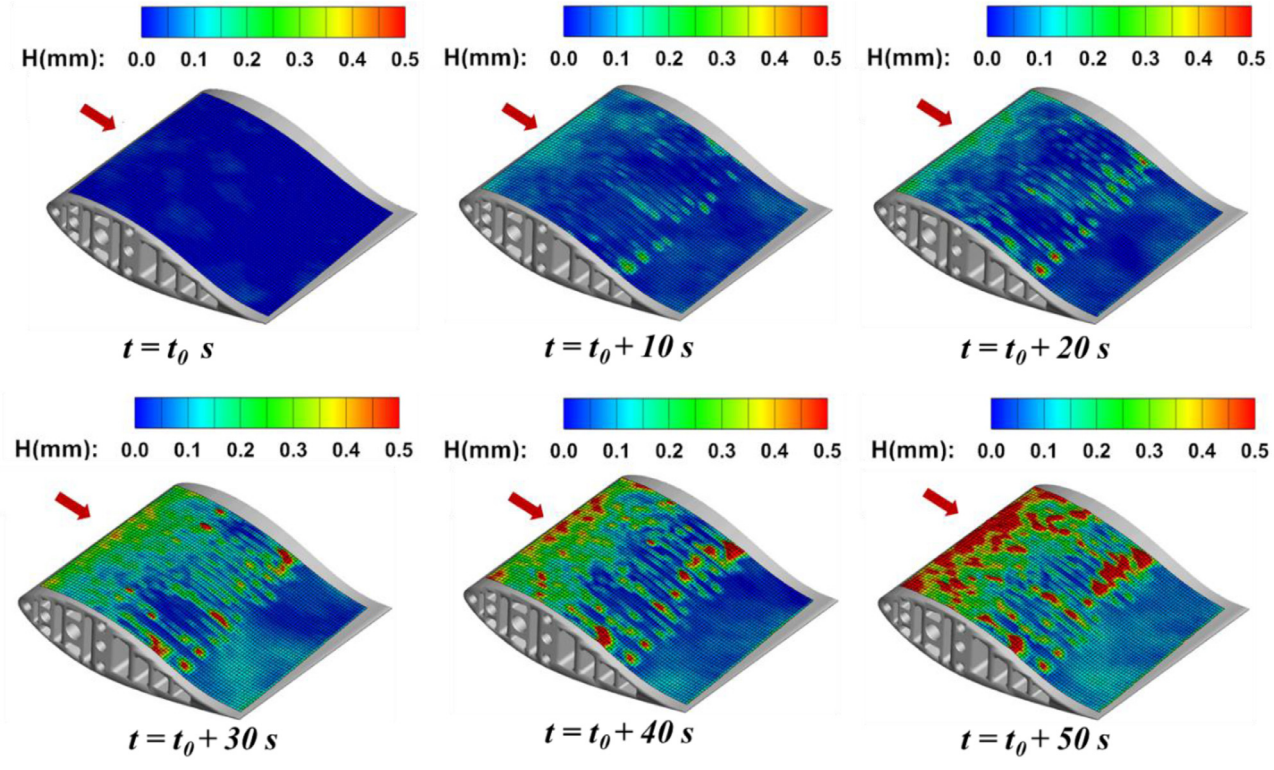

(b) DIP measurement results with V_∞ = 30 m/s.

Fig. 6. DIP measurement results to reveal the time evolutions of the dynamic glaze icing processes over the pressure-side surface of DU91-W2-250 airfoil model with AoA = 5° at two typical incoming airflow velocities.

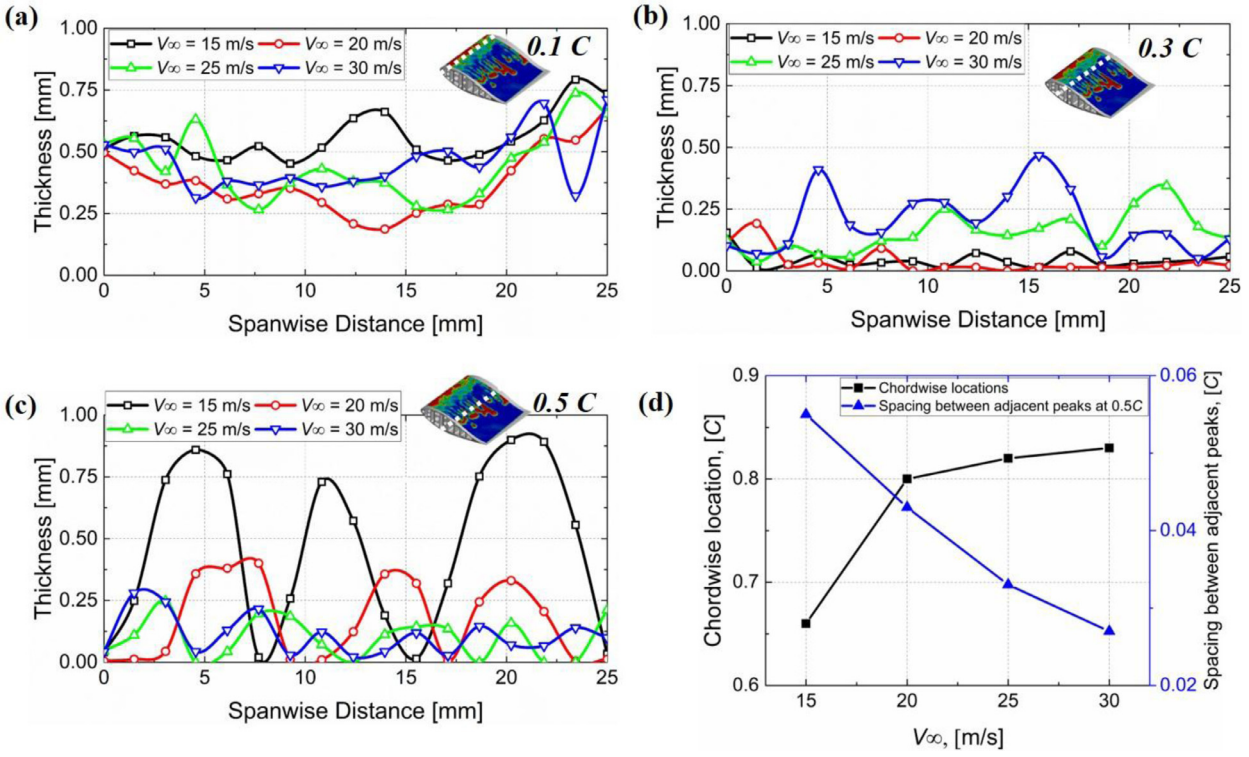

Fig. 7. Transverse profiles of water/ice thickness at three typical chordwise locations with various airflow velocities from 15 m/s to 30 m/s measured at $t = t_0 + 50$ s. (a) 0.1 *C*; (b) 0.3 *C*, (c) 0.5 *C*; and (d) Rivulet dimensions normalized by the chord length (*C*) of the airfoil model.

surface tension and shear stress at water-air interface as given in Al-Khalil et al. [35], the film front would split into isolated rivulets. As time went on to $t = t_0 + 20$ s, the rivulets extended to the further downstream region with complicated breaking and merging behaviors. Thicker ice structures were observed near the leading-edge region, i.e., the direct impinging region. At $t = t_0 + /30$ s, the ice/water accreted over the airfoil surface was continuously replenished by the subsequent water impingement and became thicker and thicker. While the water rivulets farther moved downstream, the convective heat transfer would take away the remaining latent heat of fusion in the runback water, generating the rivulets-shaped ice formation. As time went on to $t = t_0 + 40$ s, the heads of the rivulets were found to freeze and be difficult to be farther stretched along the airfoil surface by the wind-driven boundary layer airflow. As time went on to $t = t_0 + 50$ s, the rivulet heads became thicker, wider and even merged with the adjacent rivulets. Larger icicles were observed to be built up compactly along the leading edge of the airfoil model, hindering the consecutive water runback. Similar phenomena were observed in the literature [7,36].

Similar dynamic icing processes were also observed for the cases with higher velocities, i.e., at 20 m/s, 25 m/s and 30 m/s investigated in the present study. In comparison to the case with an airflow velocity of 15m/s, more rivulets were prone to form in the cases with higher inflow velocities, as shown in Fig. 6(b) where $V_\infty = 30$ m/s. As the airflow velocity increased, the rivulets were found to be flatter and thinner and capable of stretching to further downstream locations. The leading-edge water/ice structures were also found to be thinner and more uniform. More intuitively quantitative information was provided in the following subsection.

3.2. Water transport behavior over ice roughness

Fig. 7 shows the transverse profiles of the water/ice thickness at three typical chordwise locations, i.e., 0.1 *C*, 0.3 *C*, and 0.5 *C* downstream, along the airfoil surface and the rivulet dimensions under various inflow velocities ranging from 15 m/s to 30 m/s at $t = t_0 + 50$ s. It should be noted that the same amount of water was used in all the test cases with a fixed flowrate of 1000 mL/min during the experiments and thus the water collection in each case were supposed to be similar. As shown in the Fig. 7(a), the thickness of the ice/water structures accreted near the leading-edge region, i.e., 0.1 *C* along the airfoil, was found to vary slightly in the spanwise direction without showing evident periodicity. Similar phenomenon was observed at 0.3 *C*, as shown in Fig. 7(b), where in between of the leading-edge region and isolated rivulets. The average thickness of the ice/water structures at 0.1 *C* was found to be higher that at 0.3 *C* due to the higher water collection rate caused by the direct impingement of the water droplets. At 0.3 *C*, the average thickness of ice/water structures was found to be slightly higher in the case with an airflow speed of 30 m/s than that of other cases with lower airflow speeds, indicating a better chord-wise uniformity in the higher wind speed case. The *Ra* values (i.e., arithmetic average of the roughness) of roughness of water/ice structures accreted over the airfoil surface were 0.187, 0.175, 0.168, 0.145 for the cases with inflow velocities from 15 m/s to 30 m/s, respectively. Namely, as the incoming airflow velocity increased, more uniform ice/water structures (i.e., lower roughness) would be accreted over the airfoil surface.

The runback water formed many isolated rivulets whose heads were found to stop further moving downstream after a short period of time (i.e., ~30 s for all the cases). The dimensions of the rivulets could be represented by their height/thickness, length, and the spacing between the adjacent peaks (i.e., spanwise locations of the maximum heights of rivulets). In comparison to the ice/water distribution shown in Fig. 7(a) and Fig. 7(b), an evident periodicity was observed in the ice/water structure distribution at 0.5 *C* due to the isolated rivulets, as given in Fig. 7(c). After a 50-s icing process, the rivulets were found to merge with the adjacent rivulets so that no obvious gaps were observed. As the incoming airflow velocity increased, the maximum/average height of the rivulets and

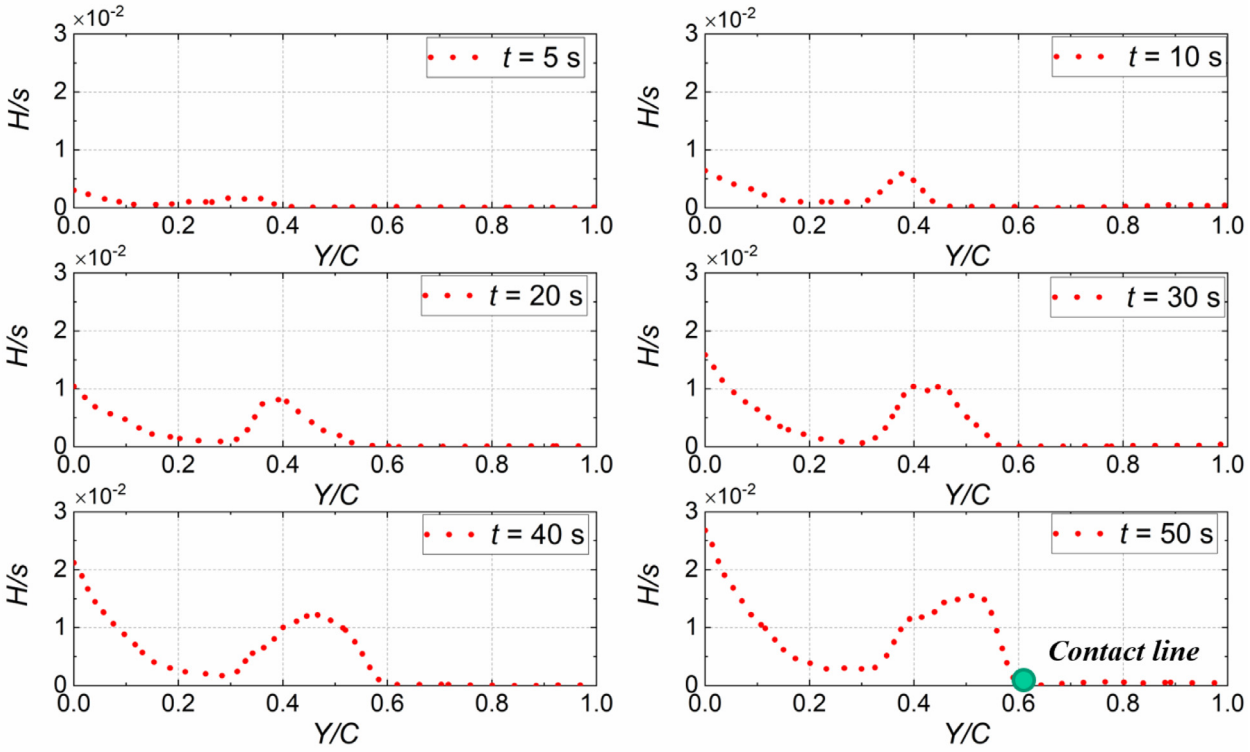

Fig. 8. Time evolutions of the water/ice thickness over the airfoil surface along the streamwise direction when V_∞ = 15 m/s and AoA = 5°.

spacing between the adjacent rivulets were found to decrease. In comparison to the case with a wind speed of 15 m/s, the spacing between adjacent peaks of rivulets in the cases with airflow velocities of 20 m/s, 25 m/s and 30 m/s were found to monotonously decrease by approximately 22%, 40%, and 51%, respectively, as shown in Fig. 7(d). The maximum/average thickness (H) of the isolated rivulets were found to decrease as the wind speed (V_∞) increased, which could be well fitted by a power function ($H = a/V_\infty{}^b$. where b ≈ 1.9) with the power-law exponent being about 2.0. Namely, the thickness of water/ice rivulets over the airfoil surface was approximately proportional to the reciprocal of the wind speed squared, and more explanations could be found in the following theoretical model. As the airflow velocity increased from 15 m/s to 20 m/s, the farthest chord-wise locations of the rivulets increased from 0.66 C to 0.80 C. As the airfoil velocity continued increasing from 20 m/s to 25 m/s, and 30 m/s, the farthest chord-wise locations of the rivulets slightly increased from 0.80 C to 0.82 C and 0.83 C, as shown in Fig. 7(d), indicating that the wind-driven rivulets could reach farther downstream locations as wind speed increased due to the higher aerodynamic force acting on them.

In the present study, based on the time sequence of the DIP measurement results as those shown in Fig. 6, the spanwise-averaged thickness/height of the water film or/and ice layer accreted over the surface of the airfoil model was obtained (i.e., averaging the measured water/ice thickness distribution along a spanwise length of 100 mm within the DIP measurement window) in order to reveal the characteristics of the dynamic glaze ice accreting process over the test model more clearly and quantitatively. Fig. 8 shows some of the spanwise-averaged thickness/height profiles of the water film or/and ice layer accreted over the pressure-side surface of the airfoil model with the airflow velocity of V_∞ = 15 m/s. In the plot, the streamwise location was normalized by the chord length of the airfoil model. As described in Battisti [33], the droplet impingement limits for an airfoil can be characterized by the upper and lower surface tangent trajectories, and the limits should be within the maximum transverse dimension of the airfoil, i.e., the maximum thickness of the airfoil. Since the present study only focused on the glaze ice accretion process over the pressure-side surface of the test model, the water/ice height/thickness over the airfoil surface was normalized by half of the maximum thickness of the airfoil model, i.e., s = 0.125 C.

Fig. 8 shows the time evolutions of the water/ice thickness over the airfoil surface along the streamwise direction when V_∞ = 15 m/s and AoA = 5°. In the very beginning of the icing process when $t = t_0 + 5$ s, the impinged water onto the airfoil surface continued solidifying with tremendous latent heat of fusion releasing during the icing process. Since the heat transfer process over the airfoil surface under such a wet icing condition would not be able to remove/dissipate all the released latent heat of fusion immediately, only a portion of the impinged water droplets would be solidified and frozen into ice upon impact (i.e., leading-edge ice accretion), while the rest of the impinged water would stay in liquid state, and as able to flow freely over the airfoil surface. The runback water, particularly a tiny bulge shape of rivulet head, was observed at approximately 0.4 C downstream position. At $t = t_0 + 10$ s, the leading-edge water/ice thickness slightly increased with the subsequent impinging water droplets, and the runback rivulet driven by the airflow moved further downstream. As time went on to 20 s, the rivulet with a budge head stretched to a farther downstream location, and the ice accretion near the leading-edge region dramatically increased, which are the major two features of a dynamic glaze icing process. When $t = t_0 + 30$ s, the contact line of the rivulet head was found to stay at a relatively fixed location, i.e., approximately 0.6 C. The runback water continued accumulating on top of the ice layer, leading to a significant increment of the water/ice thickness over the airfoil surface. After a 50-s glaze icing process, it was found that more ice structures were accreted near the leading-edge region due to the direct impingement, i.e., large water collection efficiency, and the rivulet-head region due to the wind-driven runback water.

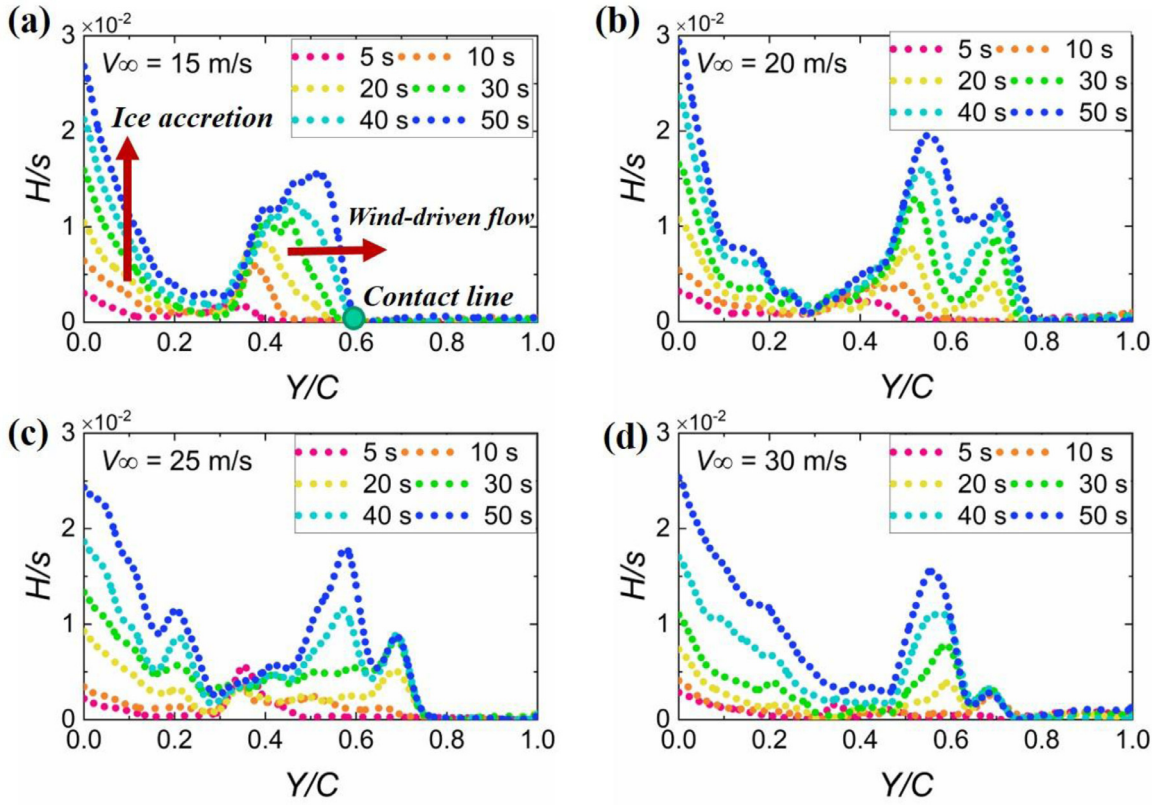

Fig. 9. Comparison of the time evolutions of the water/ice thickness over the airfoil surface along the stream-wise direction among the cases with various airflow velocities from 15 m/s to 30 m/s at AoA = 5°.

Fig. 9 compares the time evolutions of the thickness/height of the water/ice structures among the cases with different airflow velocities when AoA = 5°. As the airflow velocity increased, the contact line was found to be located at a farther downstream location. Near the leading-edge region, the thickness of the ice/water was found to increase monotonously. In the meanwhile, as the airflow velocity increased, the water runback became more complicated, represented by the multiple peaks observed in Fig. 9(b)–(d). One obvious peak was found to be located near 0.55 C (i.e., the streamwise location of the maximum thickness of the runback water) in all the cases. Another evident peak was observed farther downstream when the velocity was higher than 15 m/s. This phenomenon was found to be mainly caused by the stumbling motions of the wind-driven rivulet flows over airfoil surface. When velocity was 15 m/s, the ratio of aerodynamic force and surface tension restrain (i.e., F_d/F_c) estimated by using Eqs. (4) and (5) was found to be ~0.87 at $t = t_0 + 50$ s, indicating that the aerodynamic force was not strong enough to break the restrain due to surface tension. Therefore, the rivulet front (i.e., the contact line) could not be pushed farther over the airfoil surface and stopped at 0.55 C (the location corresponding to the maximum thickness of the rivulet head). As the airflow velocity increased, the aerodynamic force correspondingly increased, making the rivulet move farther before freezing.

In order to have a better understanding of the rivulet flow phenomena, following the work of Zhang and Hu [36], a force analysis was conducted to investigate the relationship between the ice/water structures and the airflow velocity. The bulged shapes of the runback rivulet heads could cause shape-induced aerodynamic stress when the rivulets were moving over the surface driven by the airflow. In a neutral equilibrium state, surface tension restrain equals to the sum of aerodynamic drag and water static pressure [36], as shown in Eq. (3).

$$F_c = P + F_d \tag{3}$$

where F_c is the capillary force induced by surface tension, as given in Eq. (4), and P is the water static pressure due to the boundary flow within the water layer. In the present study, the average Weber number (i.e., We, usually used to evaluate the water's inertia compared to its surface tension) of the rivulet flows in all cases was found be quite small (i.e., $We \approx 3.1 \times 10^{-4}$), and thus the effect of water static pressure was assumed to be negligible in the following calculation. F_d is the aerodynamic force that provides power for the runback water to move downstream, which is proportional to the square of airflow velocity, i.e., ${V_\infty}^2$, as given in Eq. (5).

$$F_c = W\sigma(1 - \cos\theta) \tag{4}$$

where W is the width of the rivulet, θ is the contact angle of the rivulet head (average value of ~65° in the present study), and σ is the surface tension.

$$F_d = C_f \cdot \frac{1}{2}\rho_a V_\infty^2 A_1 + C_d \cdot \frac{1}{2}\rho_a V_\infty^2 A_2 \tag{5}$$

where C_f is the friction coefficient, which equals to $0.027/Re^{1/7}$ for turbulent boundary flows over a plate [37] and Re is the chord-length based Reynolds number. In the present study, Re has magnitudes in order of 10^5 and thus C_f is quite small and negligible (i.e., less than 0.0045, ~0.7% of C_d) in all cases. C_d is the shape-induced drag coefficient for a wind-driven bead, which equals to 0.6 for airflow past a rigid hemisphere lying on a surface, as recommended by McAlister et al. [38]. A_1 and A_2 represent the friction drag affected area and the shape-induced drag acting area, respectively. A_1 and A_2 are usually assumed to have similar values (i.e.,

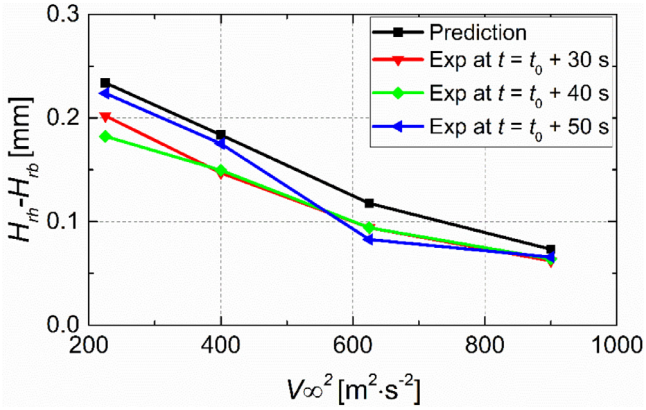

Fig. 10. A comparison between the predicted results derived from the theoretical model and the DIP measurement data of the ice/water rivulets over the pressure-side surface of the airfoil model at AoA = 5°.

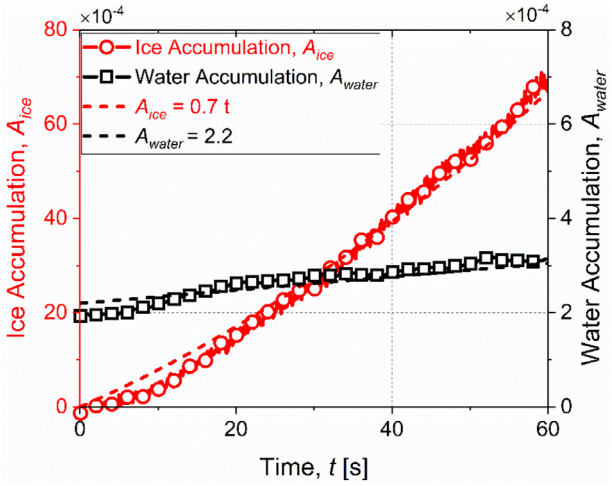

Fig. 11. Ice/water accumulation as a function of icing time.

the maximum cross section of the sphere) for a spherical bead. In the present study, A_2 was estimated by using the difference between the heights of the rivulet head and body, as well as the width of the rivulet (W), as given in Eq. (6).

$$A_2 = (H_{rh} - H_{rb})W \tag{6}$$

where H_{rb} and H_{rh} represent the height of the rivulet body and the height of the rivulet head, respectively. The smallest thickness and the highest thickness of a rivulet were used for the heights of the rivulet body and head, respectively.

Based on Eqs. (3) to (6), a relationship between the height/thickness of the rivulet flow and the airflow velocity was found, as shown in Eq. (7). The height difference between the rivulet head and body was inversely proportional to the square of the airflow velocity.

$$(H_{rh} - H_{rb}) = \frac{2\sigma(1-\cos\theta)}{\rho_a C_d V_\infty^2} \tag{7}$$

Fig. 10 shows the comparison between the predicted results derived from the theoretical model (i.e., Eq. (7)) and the DIP measurement data of the ice/water rivulets over the pressure-side surface of the airfoil model at AoA = 5°. The model was found to have a reasonably good agreement with the experimental data. As the magnitude of velocity-squared increased, the value of (H_{rh}-H_{rb}) would decrease correspondingly. The slight overestimate of (H_{rh}-H_{rb}) was suggested to be caused by the accumulative effects of the accreted budged ice structures underneath the rivulets flows. It should be noted that the theoretical model was established based on the force balance analysis of the wind-driven rivulet flows over the airfoil surface, and thus the theoretical model should be used after the icing process became steady ($t > t_0 + 30$ s). In addition, the theoretical model was built based on the force analysis of the wind-driven rivulet flows over a surface without considering the effects of AoA. The theoretical model can be applied to predict of the ice structures accreted over an airfoil surface in the cases where AoA is small and it needs be optimized for the applications for the large AoA cases (i.e., AoA > 5°).

3.3. Quantification of ice accretion

To have a better quantification of the ice/water structures accreted over the airfoil surface during dynamic icing processes, the total amount of the water and ice mixture was calculated based on the DIP measurement data and further normalized by the chord length (C) and half of the maximum thickness (s = 0.125 C) of the airfoil model, as shown in Eq. (8). To decouple water with ice, a post-processing of the DIP measurement results was conducted based on the thickness information of ice/water in two successive images. The wind-driven water would move due to the ambient airflow while the ice structures would stay on the surface. The differences between the two successive images were identified and calculated based on two types of method. In Method I, all the different regions in the two successive images were counted, which might slightly overestimate the amount of water. In Method II, only the differences of the heights in i^{th} image lower than those of the previous (i-1)th image were counted, which might slightly underestimate the amount of water. The final amount of water was defined by the average value of results calculated by those two methods. The amount of ice was defined as the difference between the total amount of water and ice and the amount of water. The amount of water and the amount of ice were also normalized by using the chord length (C)and half of the maximum thickness of the model (s = 0.125 C). It should be noted that since the water layer was quite thin and would soon freeze into ice locally if it couldn't be driven by the ambient airflow and thus the water that couldn't be driven by the airflow was not taken into account in the estimation. In addition, the effects of the time step values of the successive two images were evaluated by comparing the results calculated based on 30 Hz, 10 Hz, 1.0 Hz, 0.5 Hz and 0.1 Hz datasets. The 30 Hz datasets and 10 Hz datasets were found to be able to derive almost the same results. For the datasets with a framerate lower than 1 Hz, as the time step (1/framerate) increased, the differences between the successive two images increased, inclined to overestimate the water accumulation, because the differences caused by ice accretion were wrongly counted by using Method I. Therefore, the 30 Hz datasets were used for the calculation.

Fig. 11 shows the normalized amount of water (A_{water}) and ice (A_{ice}) as a function of time. The fitting curves for water and ice accumulation were also provided. As the ice accretion time went on, the water accumulation was found to increase slightly, mainly caused by the slightly increased impacted area of the airfoil with ice accretion. The increment of water was negligible in comparison to the amount of ice accumulation. As the ice accretion time went on, the ice accumulation was found to increase almost linearly, indicating more and more water was solidified. At $t = t_0 + 30$ s, the freezing rate (i.e., the ratio of A_{water} to A_{ice}) was less than 10.0%. As time went on to 60 s, the freezing rate (A_{water}/A_{ice}) further decreased to less than 4.0%, indicating that the water transport behaviors no longer dominated in course of the dynamic glaze ice accretion process.

$$A_c = \frac{\int_{LE}^{TE} H(y)dy}{s \cdot C} \tag{8}$$

4. Conclusions

In the present study, an experimental investigation was conducted to quantitatively measure water transport behaviors over the ice accreting surface of a wind turbine airfoil during dynamic glaze icing processes in the Icing Research Tunnel at Iowa State University (ISU-IRT). A digital image projection (DIP) technique was, for the first time, applied and verified to measure the time-resolved three-dimensional information of the ice structures and the water transport behaviors over the highly-cambered surface of the airfoil model (i.e., the pressure-side surface of DU91-W2-250 model). The stumbling motions of the rivulet flows, as well as the increased fluctuations induced by the underneath ice roughness, were well captured in the DIP measurement results.

The experiments with incoming flow velocities ranging from 15 m/s to 30 m/s were performed to study the effects of the incoming airflow velocity on the dynamic glaze icing process. It was found that, as the incoming flow velocity increased, the runback rivulet flows would move farther downstream and became thinner and narrower due to the increased aerodynamic stress acting on the rivulet flows. A theoretical model based on the force balance analysis of the rivulet flows was formulated and validated by comparing with the DIP measurement results in the present study. According to the theoretical model and experimental data, the rivulet bulged shapes were found to have an inverse relationship with the inflow velocity squared. It should be noted that, the proposed theoretical model was be applicable to the rivulet flows over the surface of an airfoil at small angles of attack (AoAs). Further investigations will be conducted in future to introduce the AoA as a parameter in the theoretical model to enlarge its applicable range to larger AoAs.

In addition, the ice structures accreted over the airfoil surface were quantitatively decoupled from the unfrozen wind-driven water during the dynamic icing process. Based on the decoupled information of ice and water, the freezing rate (i.e., A_{ice}/A_c, where $A_c = A_{ice} + A_{water}$) of an icing process could be derived and thereby used for ice accretion modelling. The experimental data, for example, the thickness distribution of ice/water structures over the airfoil surface, could be utilized for the validation and optimization of the ice accretion/water runback flow models. In the meanwhile, the amount of ice/water structures accreted over the airfoil model could be used to estimate the ice distribution over a rotating wind turbine blade by using blade element momentum (BEM) theory, which could further provide a fundamental insight to the future development of effective and robust anti-/de-icing strategies for wind turbines in cold and wet weathers.

Declaration of Competing Interest

We confirm that the manuscript has been read and approved by all named authors and that there are no other persons who satisfied the criteria for authorship but are not listed.

Acknowledgments

This research work is partially supported by Iowa Energy Center for Wind Turbine Icing Study under the IEC Competitive Grant # 312350 and National Science Foundation (NSF) under award numbers of CMMI-1824840, OISE-1826978 and CBET.

References

[1] IEA, Wind Energy in Cold Climates Available Technologies, 2016, pp. 1–119. report.
[2] T. Laakso, Wind energy projects in cold climates, Wind Energy (2005) 1–36.
[3] I. Baring-Gould, R. Cattin, M. Durstewitz, M. Hulkkonen, A. Krenn, T. Laakso, A. Lacroix, E. Peltola, G. Ronsten, L. Tallhaug, T. Wallenius, Wind Energy Projects in Cold Climates, (2012) 1–43. http://ieawind.org/index_page_postings/June7 posts/task 19 cold_climate_ rp_approved05.12.pdf.
[4] M.C. Homola, Impacts and causes of icing on wind turbines, Work (2005).
[5] L. Gao, Y. Liu, H. Hu, An experimental investigation of dynamic ice accretion process on a wind turbine airfoil model considering various icing conditions, Int. J. Heat Mass Transf. 133 (2019) 930–939, doi:10.1016/j.ijheatmasstransfer.2018.12.181.
[6] L. Gao, Y. Liu, H. Hu, An experimental study on icing physics for wind turbine icing mitigation, in: 35th Wind Energy Symp. 2017, 2017, pp. 1–16, doi:10.2514/6.2017-0918.
[7] R.M. Waldman, H. Li, H. Guo, L. Li, H. Hu, An experimental investigation on the effects of surface wettability on water runback and ice accretion over an airfoil surface, in: 8th AIAA Atmos. Sp. Environ. Conf., 2016, pp. 1–16, doi:10.2514/6.2016-3139.
[8] N. Dalili, A. Edrisy, R. Carriveau, A review of surface engineering issues critical to wind turbine performance, Renew. Sustain. Energy Rev. 13 (2009) 428–438, doi:10.1016/j.rser.2007.11.009.
[9] E. Sagol, M. Reggio, A. Ilinca, Issues concerning roughness on wind turbine blades, Renew. Sustain. Energy Rev. 23 (2013) 514–525, doi:10.1016/j.rser.2013.02.034.
[10] N. Bose, Icing on a small horizontal-axis wind turbine - Part 2: three dimensional ice and wet snow formations, J. Wind Eng. Ind. Aerodyn. 45 (1992) 87–96, doi:10.1016/0167-6105(92)90007-W.
[11] N. Bose, Icing on a small horizontal-axis wind turbine - Part 1: glaze ice profiles, J. Wind Eng. Ind. Aerodyn. 45 (1992) 75–95.
[12] R.K. Jeck, Representative values of icing-related variables aloft in freezing rain and freezing drizzle, 34th Aerosp. Sci. Meet. Exhib, 1996, doi:10.2514/6.1996-930.
[13] J.V. Cortinas, B.C. Bernstein, C.C. Robbins, J.W. Strapp, An analysis of freezing rain, freezing drizzle, and ice pellets across the United States and Canada: 1976-90, Weather Forecast 19 (2004) 377–390.
[14] H. Seifert, Technical requirements for rotor blades operating in cold climate, Proc. Boreas. VI (2003) 50–55.
[15] O. Parent, A. Ilinca, Anti-icing and de-icing techniques for wind turbines: critical review, Cold Reg. Sci. Technol. 65 (2011) 88–96, doi:10.1016/j.coldregions.2010.01.005.
[16] O. Fakorede, Z. Feger, H. Ibrahim, A. Ilinca, J. Perron, C. Masson, Ice protection systems for wind turbines in cold climate: characteristics, comparisons and analysis, Renew. Sustain. Energy Rev. 65 (2016) 662–675, doi:10.1016/j.rser.2016.06.080.
[17] L. Gao, Y. Liu, H. Hu, An experimental investigation on the dynamic ice accretion process over the surface of a wind turbine blade model, in: 9th AIAA Atmos. Sp. Environ. Conf. 2017, 2017, pp. 1–18, doi:10.2514/6.2017-3582.
[18] A.P. Rothmayer, J.C. Tsao, Water film runback on an airfoil surface, 38th Aerosp. Sci. Meet. Exhib, 2000, doi:10.2514/6.2000-237.
[19] T. Keith Jr, J. De Witt, Further development of an anti-icing runback model, 29th Aerosp. Sci. Meet, 1991, doi:10.2514/6.1991-266.
[20] K.M. Al-Khalil, T.G. Keith, K.J. De Witt, Development of an improved model for runback water on aircraft surfaces, J. Aircr. 31 (1994) 271–278, doi:10.2514/3.46484.
[21] G. Fortin, A. Ilinca, J.L. Laforte, V. Brandi, Prediction of 2D airfoil ice accretion by bisection method and by rivulets and beads modeling, 41st Aerosp. Sci. Meet. Exhib, 2003, doi:10.2514/6.2003-1076.
[22] H. Hu, B. Wang, K. Zhang, W. Lohry, S. Zhang, Quantification of transient behavior of wind-driven surface droplet/rivulet flows using a digital fringe projection technique, J. Vis. 18 (2015) 705–718, doi:10.1007/s12650-014-0264-8.
[23] K. Zhang, T. Wei, H. Hu, An experimental investigation on the surface water transport process over an airfoil by using a digital image projection technique, Exp. Fluids 56 (2015) 1–16, doi:10.1007/s00348-015-2046-z.
[24] K. Zhang, J. Blake, R. Alric, H. Hu, An experimental investigation on wind-driven rivulet/film flows over a NACA0012 airfoil by using digital image projection technique, in: 52nd Aerosp. Sci. Meet, 2014, pp. 1–9, doi:10.2514/6.2014-0741.
[25] Y. Liu, K. Zhang, H. Hu, An experimental investigation on the water runback process over an airfoil surface with realistic ice roughness, 8th AIAA Atmos. Sp. Environ. Conf., American Institute of Aeronautics and Astronautics, 2016, doi:10.2514/6.2016-3140.
[26] L. Gao, Y. Liu, W. Zhou, H. Hu, An experimental study on the aerodynamic performance degradation of a wind turbine blade model induced by ice accretion process, Renew. Energy 133 (2019) 663–675, doi:10.1016/j.renene.2018.10.032.
[27] L. Gao, Y. Liu, H. Hu, Quantification of dynamic glaze icing process over an airfoil surface by using a digital image projection (DIP) technique, in: 2018 Atmos. Sp. Environ. Conf., 2018, pp. 1–13, doi:10.2514/6.2018-3829.
[28] R.P.J.O.M. Van Rooij, W.A. Timmer, Roughness sensitivity considerations for thick rotor blade airfoils, in: ASME 2003 Wind Energy Symp. Wind, 125, 2003, pp. 22–31, doi:10.1115/1.1624614.
[29] W. a. Timmer, R. Van Rooij, Some aspects of high angle-of-attack flow on airfoils for wind turbine application, in: EWEC 2001, 125, Copenhagen, Denmark, 2001, pp. 4–7, doi:10.1115/1.1626129.
[30] L. Gao, R. Veerakumar, Y. Liu, H. Hu, Quantification of the 3D shapes of the ice structures accreted on a wind turbine airfoil model, J. Vis. (2019), doi:10.1007/s12650-019-00567-4.
[31] R.M. Waldman, H. Hu, High-speed imaging to quantify transient ice accretion process over an airfoil, J. Aircr. 53 (2016) 369–377, doi:10.2514/1.C033367.

[32] A. Hudecz, Icing problems of wind turbine blades in cold climates, DTU (2014).
[33] L. Battisti, Wind Turbines in Cold Climates, 2015. doi:10.1007/978-3-319-05191-8.
[34] Y. Liu, H. Hu, An experimental investigation on the unsteady heat transfer process over an ice accreting airfoil surface, Int. J. Heat Mass Transf. 122 (2018) 707–718, doi:10.1016/j.ijheatmasstransfer.2018.02.023.
[35] K.M. Al-Khalil, T.G. Keith, K.J. De Witt, Development of an anti-icing runback model, 28th Aerosp. Sci. Meet. 1990, 1990 doi:, doi:10.2514/6.1990-759.
[36] K. Zhang, H. Hu, An experimental study on the transient behavior of wind-driven water runback over a flat surface, 54th AIAA Aerosp. Sci. Meet, 0, 2016 doi:, doi:10.2514/6.2016-1123.
[37] M.T. Boyle, C. Knaub, Low Speed Wind Tunnel Testing, Third Ed., Wiley & Sons, 1988.
[38] G. McAlister, R. Ettema, J.S. Marshall, Wind-driven rivulet breakoff and droplet flows in microgravity and terrestrial-gravity conditions, J. Fluids Eng. Trans. ASME 127 (2005) 257–266, doi:10.1115/1.1881696.